Polarimetric and Dual-Doppler Radar Observations of the Lipscomb County, Texas, Supercell Thunderstorm on 23 May 2002

JEFFREY FRAME, PAUL MARKOWSKI, AND YVETTE RICHARDSON

Department of Meteorology, The Pennsylvania State University, University Park, Pennsylvania

JERRY STRAKA

School of Meteorology, University of Oklahoma, Norman, Oklahoma

JOSHUA WURMAN

Center for Severe Weather Research, Boulder, Colorado

(Manuscript received 17 October 2007, in final form 30 June 2008)

ABSTRACT

Polarimetric and dual-Doppler observations of a supercell observed by the National Center for Atmospheric Research (NCAR) S-band Polarimetric (SPOL) radar, two Doppler-On-Wheels (DOW) radars, and the Greek XPOL radar on 23 May 2002 during the International H_2O Project (IHOP) are presented. The polarimetric radar observations began as the storm organized into a supercell and continued for over an hour while the storm was in its mature phase. The hydrometeor distribution within the mature storm was retrieved using a fuzzy logic hydrometeor classification algorithm. The dual-Doppler radar observations began around the time that the polarimetric radar observations concluded, and they covered the end of the mature phase and much of the dissipation phase of the storm. The dual-Doppler wind syntheses are used to evaluate the importance of the forward-flank outflow in augmenting the horizontal vorticity field near the storm above 400 m. In this case, having a relatively weak low-level mesocyclone, the parcel trajectories and the horizontal vorticity field observed within the forward-flank outflow are not what one would likely expect based on prior numerical studies (having generally stronger low-level mesocyclones) that have emphasized an important dynamical role for forward-flank downdrafts in terms of their horizontal vorticity generation. Instead, the observed trajectories could not be traced from the forward-flank outflow toward the storm's updraft and the horizontal vorticity vectors within the forward-flank outflow generally did not point (westward) toward the storm's updraft.

1. Introduction

Numerical simulations of supercell thunderstorms have suggested that horizontal buoyancy gradients near the edge of the forward-flank precipitation region (Lemon and Doswell 1979; see our Fig. 1) provide an important enhancement of low-level horizontal vorticity via baroclinic generation (e.g., Klemp and Rotunno 1983; Rotunno and Klemp 1985; Wicker and Wilhelmson 1995). This horizontal vorticity can be tilted into the vertical and subsequently stretched by the storm's updraft, and is believed to be an important source of vorticity for low-level mesocyclones. The hydrometeor distribution within a supercell, including that within the forward-flank region, may have an important effect on buoyancy and buoyancy gradients, because evaporation and melting rates, and thus the potential for latent cooling, depend heavily upon it. Herein, we document a supercell observed by a fixed dual-polarization radar and three mobile Doppler radars. From these observations, the hydrometeor and three-dimensional wind fields are retrieved, with emphasis on the forward-flank precipitation region.

Over the past decade, there have been a growing number of supercell thunderstorm studies relying heavily on mobile Doppler radar observations. A majority of the ground-based mobile radar observations have been single Doppler (e.g., Bluestein et al. 1997, 2003; Wurman

Corresponding author address: Jeffrey Frame, Department of Meteorology, The Pennsylvania State University, 503 Walker Building, University Park, PA 16802.
E-mail: jwf155@psu.edu

DOI: 10.1175/2008MWR2425.1

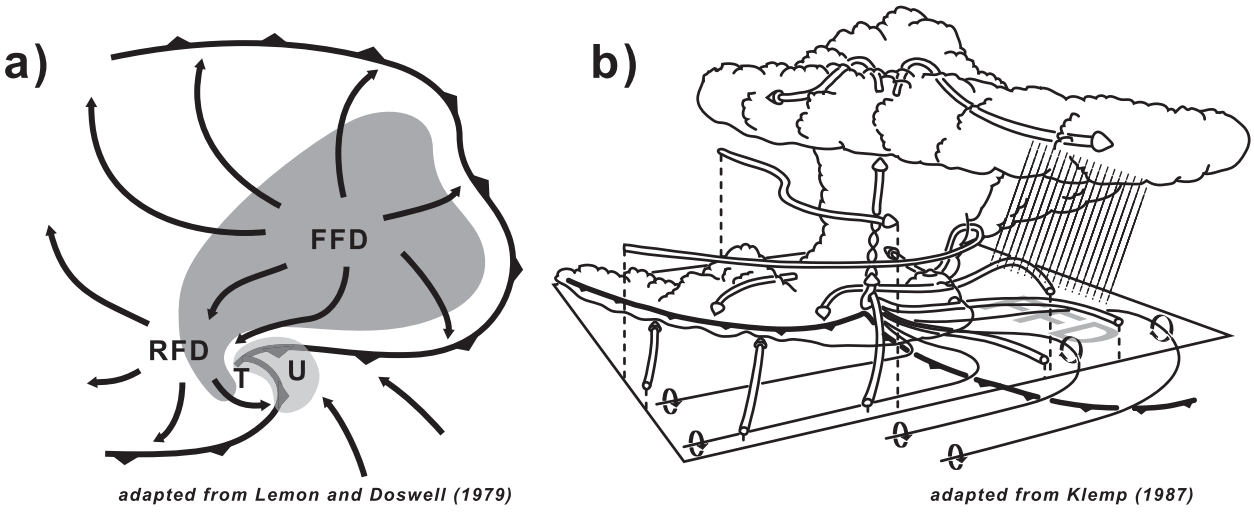

FIG. 1. (a) Schematic representation of a supercell thunderstorm, adapted from the conceptual model presented by Lemon and Doswell (1979). (b) Three-dimensional schematic of a numerically simulated supercell thunderstorm in westerly mean shear, viewed from the southeast, at a stage when low-level rotation is intensifying. The cylindrical arrows depict the storm-relative winds. The thin lines are vortex lines, with the sense of rotation indicated by the circular arrows. The heavy barbed line marks the outflow boundary. Adapted from Klemp (1987).

and Gill 2000; Alexander and Wurman 2005; Lee and Wurman 2005), with relatively few dual-Doppler studies (Beck et al. 2006; Wurman et al. 2007a,b). There also have been several airborne pseudo-dual-Doppler radar studies (e.g., Wakimoto et al. 1998, 2003; Trapp 1999; Wakimoto and Cai 2000; Ziegler et al. 2001; Dowell and Bluestein 2002) in which data within the forward flank were available, but, understandably, the supercell mesocyclone regions tended to be the focus of the investigations. Detailed examinations of ground-based, mobile Doppler radar observations, especially dual-Doppler, within the forward-flank downdraft have been limited, however, and less frequent than mobile Doppler radar studies of tornadoes themselves (Wakimoto 2001).

On 23 May 2002, two Doppler-on-Wheels (DOW) radars (Wurman et al. 1997) and the Greek XPOL radar (Wurman 2001) intercepted a supercell over the northeastern Texas Panhandle (hereinafter the Lipscomb County storm) during the International H_2O Project (IHOP_2002; Weckwerth et al. 2004). The DOW radar data are complimented by observations from the National Center for Atmospheric Research (NCAR) S-band Polarimetric (SPOL) radar (Lutz et al. 1995). The polarimetric radar data help elucidate the types of hydrometeors present within this storm's peculiar winged reflectivity signature. The dual-Doppler data permit the retrieval of the three-dimensional wind and vorticity fields within the forward flank.

An overview of the storm and its environment is contained in section 2. Section 3 describes the data and analysis methods. The polarimetric radar data are discussed in section 4. The dual-Doppler data are discussed in section 5. The conclusions can be found in section 6.

2. Storm overview

During the afternoon of 23 May 2002, a stationary front extended from south-central Kansas southwestward to an area of low pressure located over the Texas Panhandle (Fig. 2). This front separated slightly cooler but significantly drier air to its north from warmer and moister air to its south. The surface winds in the warm sector were from the southeast, but the surface winds north of the front were northeasterly. A 500-hPa trough was located over the Great Basin, and broad southwesterly flow at this level existed over much of the Great Plains (not shown).

A Local Analysis and Prediction System (LAPS) sounding from 0000 UTC 24 May near Gage, Oklahoma (Fig. 3a), reveals 1734 J kg^{-1} of convective available potential energy (CAPE) and modest convective inhibition (CIN; approximately 75 J kg^{-1}).[1] None of the standard 0000 UTC upper-air soundings are representative

[1] The CAPE and CIN calculations are for an undiluted surface parcel and include virtual temperature effects (Doswell and Rasmussen 1994). A parcel lifted having the mean potential temperature and specific humidity of the lowest 100 mb (Craven et al. 2002) would have comparable CAPE but roughly half as much CIN.

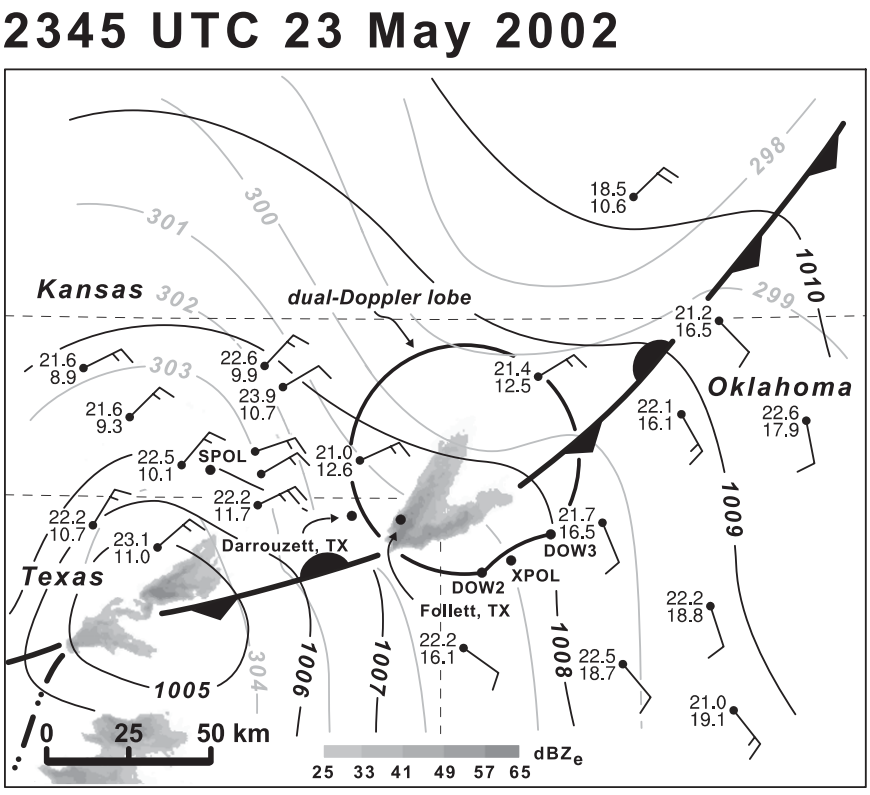

FIG. 2. Surface analysis at 2345 UTC 23 May 2002. Mean sea level pressure (black contours) and potential temperature (gray contours) are analyzed at 1-hPa and 1-K intervals, respectively. Temperature (°C), dewpoint temperature (°C), wind speed (half barb—2.5 m s^{-1}, full barb—5 m s^{-1}), and wind direction are plotted in the station models. The thick line with filled barbs and scallops indicates the stationary front, and an outflow boundary is analyzed with a dash–double-dot line. Radar reflectivity factor (dBZ_e) from the SPOL radar also is overlaid (see legend), as is the dual-Doppler lobe (thick black solid line) formed by the DOW2 and DOW3 mobile radars if a minimum interbeam angle of 20° is required (Davies-Jones 1979). The location of the XPOL radar is also shown.

of the near-storm environment: Dodge City, Kansas, to the north, was north of the surface front; Amarillo, Texas, to the southwest, was west of the moist surface air; and Norman, Oklahoma, to the southeast, was contaminated by ongoing convection. The vertical wind profile from the LAPS sounding contains 17 m s^{-1} of 0–6-km shear (Fig. 3b). The hodograph exhibits slight clockwise turning with height in the 0–1-km layer, while the shear vector is generally straight between 1 and 6 km.

The radar echo that became the Lipscomb County storm organized along the front around 2200 UTC over the northern Texas Panhandle (Fig. 4a). By 2229 UTC (Fig. 4b), the storm formed a hook echo on its right-rear flank. (Here, ''right'' is with respect to the reference frame of an observer looking along the storm-motion vector.) The storm moved just north of due east through 2301 UTC (Fig. 4c). By 2316 UTC, the forward flank of the storm took on a wing-shaped appearance (Fig. 4d), with a notch of lower reflectivity located between two wings of higher reflectivity. The reflectivity notch can also be seen earlier in the storm's evolution (Fig. 4b), but it did not become prominent until after 2316 UTC. This wing-shaped reflectivity pattern persisted for over an hour (until after 0000 UTC; Figs. 4e–g), strongly suggesting that this reflectivity pattern and accompanying notch is not the result of storm splitting, but rather is due to other internal dynamical and microphysical processes. The radar data also reveal no evidence of an anticyclonic ''left mover'' at any time during the observation period.

Around 2316 UTC, the eastward motion of the storm slowed and the storm turned right, which resulted in a motion vector directed just south of due east. The storm remained in a relatively steady state through 2346 UTC (Figs. 4e,f), with maximum reflectivity values in the

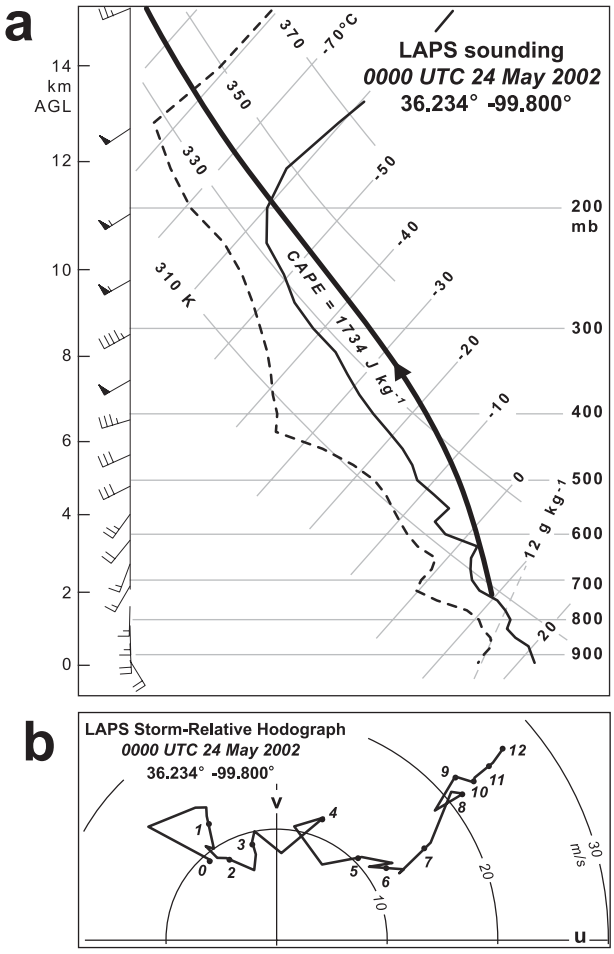

FIG. 3. (a) LAPS sounding from 0000 UTC 24 May 2002, approximately 25 km southeast of the Lipscomb County storm (cf. Fig. 4). The thick black line represents the approximate path a surface-based parcel would take. The vertical profile of the wind is shown with the half-barb, full barb, and flag representing 2.5, 5.0, and 25.0 m s^{-1}, respectively. (b) Storm-relative hodograph based on the wind profile in (a). The calculated storm motion was 5.3 m s^{-1} from 278°.

echo core exceeding 65 dBZ_e. A satellite image from 2345 UTC (Fig. 5) depicts the storm over the extreme northeastern Texas Panhandle. Also evident is the cirrus anvil, which extended over 200 km downwind from the storm's primary updraft. The reflectivity values within the echo core began to diminish by 0000 UTC (Fig. 4g). The storm weakened further by 0015 UTC (Fig. 4h), such that few echoes with reflectivities above 50 dBZ_e remained. The storm continued to dissipate after 0015 UTC.

Storm Data (NCDC 2002) indicates that this storm produced a brief, apparently insignificant (*Storm Data* reports a path width and length of 25 and 0 yd, respectively) tornado at 2330 UTC near Follett, Texas. The storm also produced 3-cm diameter hail at Darrouzett, Texas, at 2257 UTC and 5-cm diameter hail at Follett at 2330 UTC (Fig. 2). In this second report, it was noted that the hail persisted for 30 min.

3. Data and methodology

The Lipscomb County supercell was sampled by NCAR's SPOL radar, which was located in the east-central Oklahoma Panhandle in support of IHOP. Polarimetric radar data were analyzed from 2200 to 0000 UTC, after which time SPOL data collection was terminated. The polarimetric data are used to determine the hydrometeor fields using the fuzzy logic hydrometeor classification algorithm described by Straka et al. (2000) and Zrnic et al. (2001). This method is described in more detail in the appendix. This storm was later intercepted by the DOW radars and the Greek XPOL radar.[2] Data collection from these radars began around 2345 UTC and continued until the demise of the storm was imminent, at about 0040 UTC. As noted above, the storm was already beginning to weaken at 0000 UTC, which limits the overlapping dual-Doppler and SPOL observations of the mature supercell to a few minutes around 2345 UTC. The locations of the radars are shown in Fig. 5.

DOW2 scanned at 16 elevation angles, ranging from 0.4° to 14.5°, and DOW3 also scanned at 16 angles, but between 0.6° and 14.5°. These observations result in an average vertical data spacing ranging from approximately 150 to 300 m, depending on the distance from the radars. The lowest radar beams were between 300 and 600 m above ground level (AGL) within the storm.

The dual-Doppler syntheses (Fig. 4) do not include the mesocyclone and updraft of the supercell, but do cover much of the forward flank of the storm. The main updraft and attendant mesocyclone are too far removed from one of the radars (DOW3) and the interbeam angles are too small in this region of the storm to provide a trustworthy dual-Doppler analysis of the updraft or mesocyclone.[3] The baseline between DOW2 and DOW3 was 24.5 km.

[2] The XPOL radar was not included in the Doppler wind syntheses because its volume scans were not well synchronized in time with DOW2 and DOW3. Additionally, XPOL only scanned to a maximum elevation angle of 6.0°. The inclusion of data from the XPOL radar seemed to adversely affect the three-dimensional wind syntheses, probably as a result of the aforementioned scanning differences between XPOL and DOW2/3.

[3] The dual-Doppler lobe displayed in some of the figures (e.g., Fig. 4) differs from the area covered by some of the dual-Doppler syntheses because the far-western portions of the dual-Doppler lobe are below the radar horizon of DOW3 at low elevations.

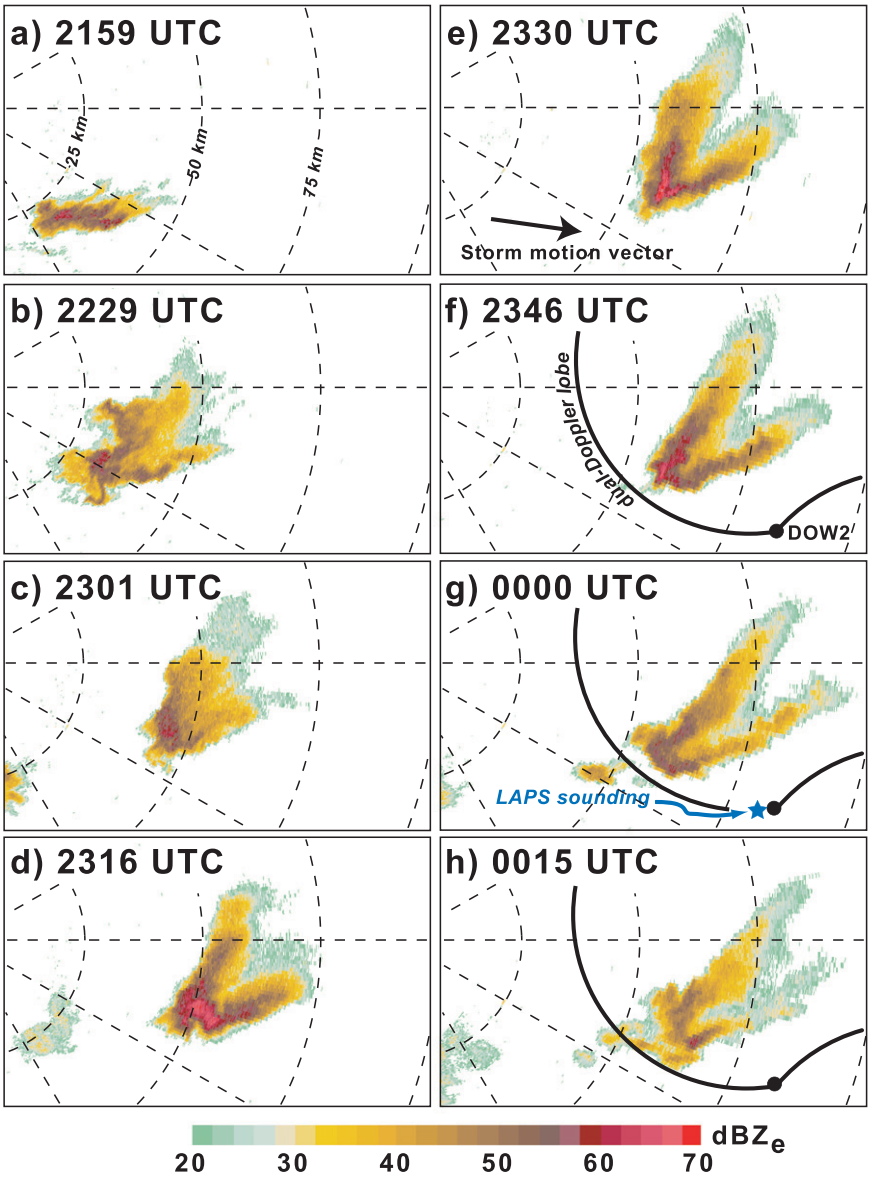

FIG. 4. Radar reflectivity factor (dBZ_e) from the SPOL radar 0.5° scan at (a) 2159, (b) 2229, (c) 2301, (d) 2316, (e) 2330, (f) 2346, (g) 0000, and (h) 0015 UTC. The southern and western edges of the dual-Doppler lobe formed by the DOW2 and DOW3 mobile radars are displayed in (f)–(h). The location of the LAPS sounding and hodograph (see Fig. 3) is indicated in (g).

Data from all of the radars were mapped to a Cartesian grid using a one-pass Barnes analysis (Barnes 1964). The SPOL grid has a horizontal and vertical grid spacing of 500 m. The Barnes smoothing parameter κ used for the SPOL data was 1.15 km^2. For the other radars, the DOW and XPOL data were objectively analyzed to a 60 × 60 × 2 km grid having a horizontal grid spacing of 250 m and a vertical spacing of 100 m, using $\kappa = 0.69$ km^2. (Even with these relatively high-resolution data, it is certain that some small-scale structures are not well-resolved, because of limitations both in the data and in the analysis techniques.) These values of κ follow from the tests of Pauley and Wu (1990), who recommended setting $\kappa = (1.3d)^2$, where d is conservatively taken to be the coarsest data spacing in this case (Trapp and Doswell 2000). The cutoff radius, used for computational expediency, was 1.8 km for the DOW and XPOL data and 2.4 km for the SPOL data. The values of κ and the cutoff radius used for the SPOL radar are larger than those used for the DOW radars because the

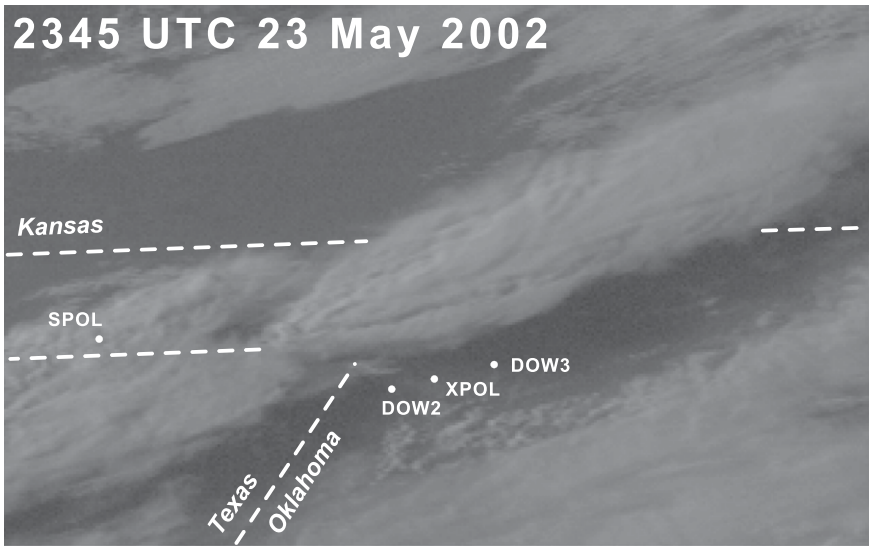

FIG. 5. Visible satellite image from *GOES-8* at 2345 UTC 23 May 2002. The locations of the SPOL, DOW2, DOW3, and XPOL radars also are shown.

SPOL radar was farther from the storm than were the DOW radars, so its data spacing is greater. A flat lower boundary was assumed in the analysis, and the bottom of the grid was defined to be at the mean elevation of the DOW2 and DOW3 radars. Because of higher terrain to the northwest of the radars, the variables analyzed herein may be at an elevation of up to 100 m closer to the ground than is indicated in the analysis.

A correction was incorporated into the analysis to compensate for the motion of the storm (5.3 m s^{-1} from 278°) during the time required to complete a volume scan (approximately 120 s for the DOW radars). The extrapolation of data into data voids was not permitted during the objective analysis, resulting in qualitatively better kinematic fields in the three-dimensional wind syntheses. The three-dimensional wind syntheses were constructed using the variational technique with weak constraints described by Gamache (1997). This variational method minimizes a cost function that considers the radial velocity projections, mass continuity, a lower boundary condition ($w = 0$ at $z = 0$), and a smoothing parameter.

4. Polarimetric radar observations

Differential reflectivity (Z_{DR}) is the logarithm of the ratio of the power returned by horizontally polarized waves (Z_{HH}) to that returned by vertically polarized waves (Z_{VV}). As such, hydrometeors with large aspect ratios (such as large raindrops) tend to return larger values of Z_{DR}, whereas more spherical hydrometeors, like hailstones and small raindrops, return values of Z_{DR} that are closer to zero. A table containing the hydrometeor types indicated by various values of polarimetric variables can be found in the appendix.

An examination of the Z_{DR} field from SPOL (Fig. 6a) reveals enhanced Z_{DR} values downwind of the precipitation core within the reflectivity wings. This enhancement is especially prominent on the northwest side of the storm, and indicates the presence of moderate to large-sized raindrops (the polarimetric hydrometeor classification algorithm is discussed in detail in the appendix). The Z_{DR} values decrease downwind of these maxima, implying that the northeastern portion of the main echo body mainly consists of smaller-sized raindrops, which is not surprising considering the distance between this portion of the storm and the updraft. There is also a Z_{DR} maximum upwind of the precipitation core, which also suggests the presence of moderate-to-large-sized raindrops in this region of the storm.

Linear depolarization ratio (LDR) is the ratio of the power returned by horizontally (vertically) polarized waves from a vertically (horizontally) polarized pulse. The amount of polarization change depends upon, among other things, the shape of the scatterer. The LDR values can distinguish between rain, small hail, large hail, or mixtures of hydrometeor types.

The high values of LDR near the echo core suggest that there is heavy rain likely mixed with hail in this region (Fig. 6b). [The presence of hail is indicated by high values of reflectivity (Z_{HH}) collocated with low

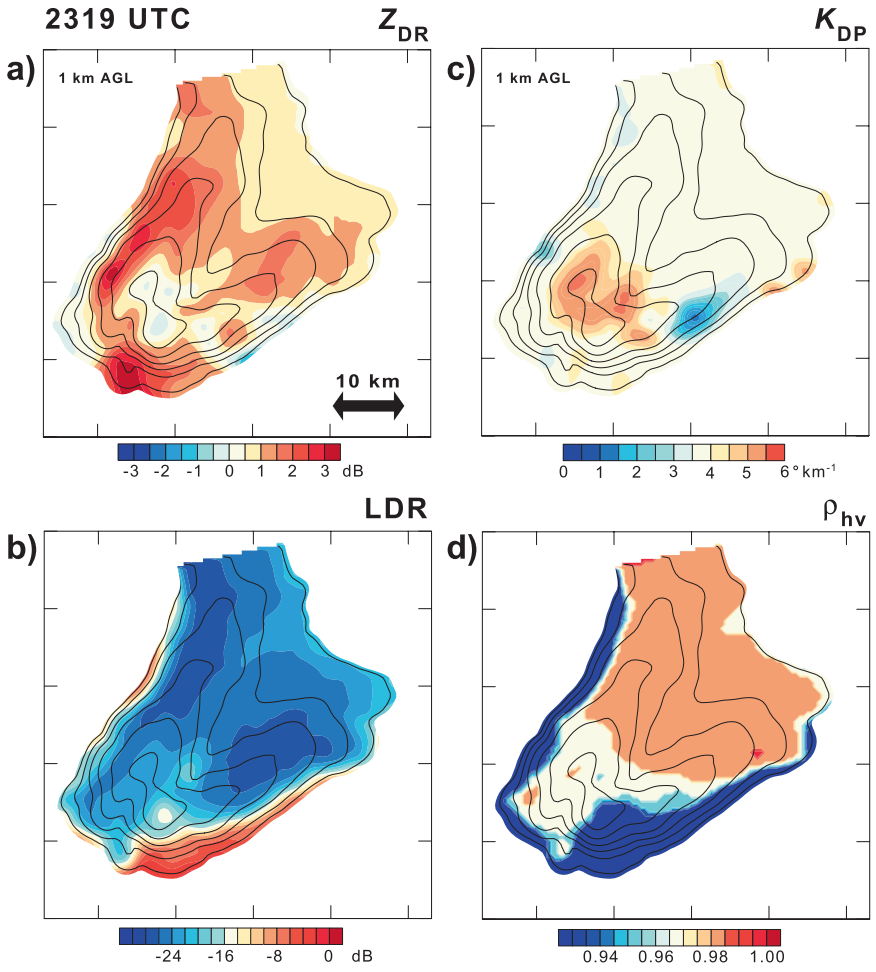

FIG. 6. Objectively analyzed SPOL polarimetric radar data at 2319 UTC 23 May 2002 at 1 km AGL (color shading): (a) differential reflectivity, Z_{DR}; (b) linear depolarization ratio, LDR; (c) specific differential phase, K_{DP}; and (d) cross-correlation coefficient between the horizontally and vertically polarized waves, ρ_{hv}. Equivalent radar reflectivity factor contours are overlaid at 10-dBZ_e intervals, starting at 10 dBZ_e.

values of Z_{DR}.] The raindrops within the core of the storm are either being shed from melting hailstones or are raindrops with partially melted hailstones in their centers. It is also possible that the raindrops could be originating from the melting of other hydrometeors. Any hailstones would likely have been 9 mm in diameter or larger, however (see the appendix). There are some signs of smaller patches of larger hail in the hail-size categorization discussed below.

Specific differential phase (K_{DP}) is the difference in the phase shift of the horizontally and vertically polarized waves due to changes in the speed of the radar pulses as they travel through hydrometeors. Large values of K_{DP} indicate the presence of hydrometeors with high water content, and values closer to zero indicate hydrometeors with small water content.

The SPOL polarimetric fields indicate small Z_{DR} values collocated with large values of K_{DP} near the echo core (Fig. 6c), which suggest the presence of a large population of medium-sized raindrops, with the possibility of a high water content in this region of the storm. It is also possible that a few hailstones are mixed in with the rain in this region. The modestly high reflectivity values collocated with the hail signature implies that any hailstones are generally small in size. This is not consistent with the two reports of hail 3–5 cm in diameter noted in section 2, however. In the wings of the reflectivity pattern, the large values of Z_{DR} and small values of K_{DP} indicate the presence of a few large raindrops, whose total population has a small liquid water content.

The cross-correlation coefficient between the horizontally and vertically polarized waves (ρ_{hv}) is generally

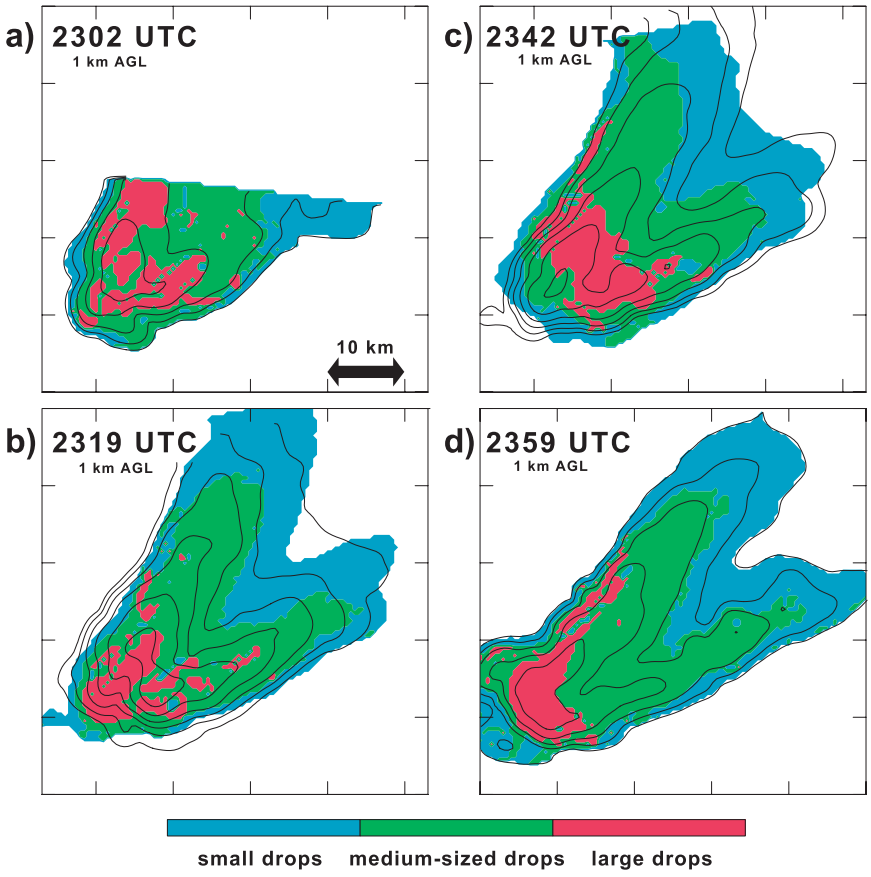

FIG. 7. Relative raindrop size fields at 1 km AGL at (a) 2302, (b) 2319, (c) 2342, and (d) 2359 UTC 23 May 2002, derived from the SPOL dual-polarimetric radar data (see legend). Equivalent radar reflectivity factor contours are overlaid at 10-dBZ_e intervals, starting at 10 dBZ_e. Note that the drop size fields in (b) were derived from the polarimetric radar data in Fig. 6.

near unity if the radar beam only encounters raindrops. Mixed precipitation types and hailstones cause this parameter to be significantly less than one because these hydrometeor species scatter vertically and horizontally polarized waves differently, which would naturally decrease the correlation coefficient between the two fields.

A plot of ρ_{hv} from SPOL (Fig. 6d) reveals high values (approaching unity) downwind of the precipitation core, implying rain in this region. Closer to the reflectivity core, the values decrease, which is consistent with the presence of a mixture of rain and hail, or larger hail (see the appendix). Also, the ρ_{hv} field is not suggesting very large hailstones anywhere in the storm.

The polarimetric hydrometeor classification algorithm (HCA; Straka et al. 2000) raindrop size distribution (Fig. 7) illustrates that raindrop size is well correlated with reflectivity. This association would be somewhat expected, however, given that Z_{HH} and Z_{DR} both factor into the HCA. Throughout the evolution of the storm, the largest raindrops are found within the precipitation core and along the left flank of the main echo body. Relatively smaller drops are indicated within the low reflectivity notch, which runs approximately along the major axis of the echo. The larger drops are predominantly located near the echo core at 2302 UTC (Fig. 7a), but larger drops are also indicated sporadically along the reflectivity wings by 2319 UTC (Fig. 7b). At 2342 UTC (Fig. 7c), there may be more hail within the reflectivity core than at other times, because the HCA does not return a large raindrop size classification within the reflectivity core. Large drops are also likely present along the echo flanks at this time. By 2359 UTC (Fig. 7d), the HCA again returns a large raindrop signature near the echo core as well as along the left flank of the storm.

The HCA hydrometeor classifications from SPOL at 1, 4, and 7 km at 2302, 2319, 2342, and 2359 UTC are consistent from time to time, and from level to level at each time (Fig. 8). At 1 km AGL, there is only rain and a rain–hail mixture present. There are also signatures of a

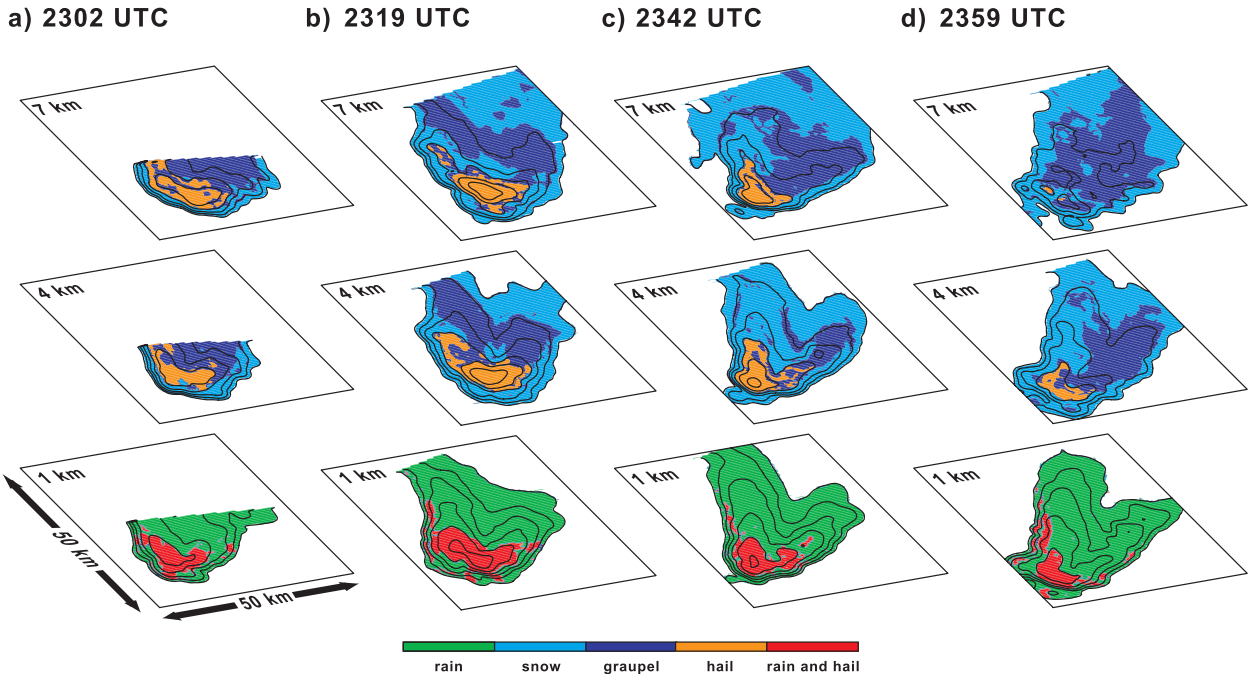

FIG. 8. Hydrometeor fields at 1, 4, and 7 km AGL at (a) 2302, (b) 2319, (c) 2342, and (d) 2359 UTC 23 May 2002, derived from the SPOL dual-polarimetric radar data (see legend). Equivalent radar reflectivity factor contours are overlaid at 10-dBZ_e intervals, starting at 10 dBZ_e. Note that the hydrometeor fields in the 1 km AGL slice in (b) were derived from the polarimetric radar data in Fig. 6.

rain–hail mixture present in the tight reflectivity gradients near and just downwind of the precipitation core. These signatures are likely false because one would not expect to find hail confined within a reflectivity gradient, while hail was not present in the nearby reflectivity wings, which contain high reflectivity. (The use of fuzzy logic in the HCA reduces, but does not eliminate misclassifications of hydrometeor types as outlined in the appendix.) At 4 km AGL, the rain–hail mix becomes all hail and is surrounded by a large region of graupel. Farther downwind, where the reflectivity is lower, there is the expected mix of graupel and snow. The hail signature at this level weakens with time near the end of the observation period. Snow and graupel prevail at 7 km AGL, and it is likely that there is no liquid water present or melting occurring at this elevation, given an updraft temperature of 0°C at 4 km AGL, assuming moist adiabatic ascent. (The ambient 0°C isotherm is at 3.5 km AGL, and the ambient 7 km temperature is −28°C.) Even at 7 km, there is a signature of hail near the reflectivity core, which also weakens with time, like that seen at 4 km.

There was a brief period of overlap in polarimetric data collection between the SPOL and XPOL radars, allowing for one of the first comparisons of polarimetric data from two different radars collected nearly simultaneously. Only Z_{DR} values are available from XPOL, and they are compared with those from SPOL (Fig. 9). Both Z_{DR} fields exhibit the same general pattern (Fig. 9), with Z_{DR} maxima located in the wings of high reflectivity and a minimum in the low-reflectivity notch. The near-zero Z_{DR} values previously seen near the echo core have disappeared by this time (cf. Figs. 6a and 9).

The SPOL Z_{DR} values are slightly lower than the XPOL Z_{DR} values in the southern echo wing (Fig. 9). This difference is likely not due to attenuation of the SPOL beam, because SPOL operates at a wavelength of 10 cm, and any attenuation of radiation by heavy precipitation at this wavelength is negligible (Doviak and Zrnic 1993, p. 42). A more likely explanation for this Z_{DR} discrepancy is that the XPOL beam significantly scatters owing to large precipitation particles within the southern echo wing (Fig. 7). Attenuation of the XPOL beam appears to be the reason for the large area of negative Z_{DR} values on the northern and western flanks of the storm (Fig. 9). Given the positive Z_{DR} values throughout most of the storm, the horizontally polarized beam was likely attenuated more than the vertically polarized beam, meaning that relatively less power was returned by the horizontally polarized beam than by the vertically polarized beam. Thus, the logarithm of the ratio of the returned power from each beam would tend toward zero, or even become negative.

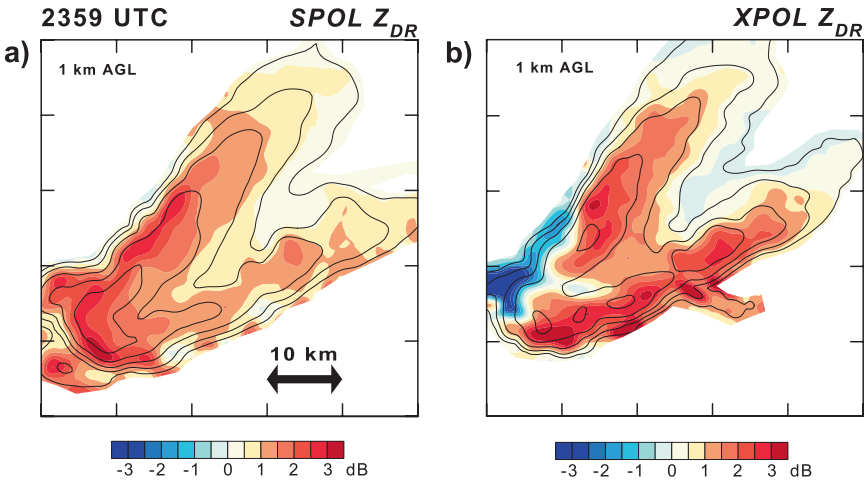

FIG. 9. Objectively analyzed differential reflectivity, Z_{DR}, at 2359 UTC 23 May 2002 at 1 km AGL (color shading) from the (a) SPOL radar and (b) XPOL radar. Equivalent radar reflectivity factor contours are overlaid at 10-dBZ_e intervals, starting at 10 dBZ_e.

Other previous polarimetric analyses of supercells bear much resemblance to the case examined herein, especially within the forward flanks of the respective storms. Ryzhkov et al. (2005) examined polarimetric data acquired in three different supercells (3 May 1999, and 8 and 9 May 2003; their Figs. 2, 5, and 9, respectively), all of which produced F2 or stronger tornadoes while being analyzed. In all three cases, it was found that significant Z_{DR} values remained below about 1.0 km AGL within the forward flanks of the storms. In both cases where a plan view near 1 km AGL was presented (the 8 and 9 May 2003 cases), the maximum values of Z_{DR} were located outside of the main reflectivity core, which matches the present case well. The values of ρ_{hv} from those two cases also closely matched those seen in this case (a radar calibration error in the remaining case rendered those ρ_{hv} values untrustworthy). The storms of 3 May 1999 and 8 May 2003 also contained a maximum in ρ_{hv} within the main echo body that was near, but not collocated with the highest reflectivity values. It could not be determined whether this was the case in the 9 May 2003 storm. A hydrometeor classification was not attempted in that study, and the only variables presented were reflectivity, single-Doppler velocity, Z_{DR}, and ρ_{hv}.

A later study by Heinselman and Ryzhkov (2006) presented selected polarimetric fields and attempted a hydrometeor classification (see their Fig. 3) for a storm that occurred on 19 May 2003. This storm did not appear to be as well organized as those mentioned above, but it still contained a sharp reflectivity gradient on its right flank, much like the storm of 23 May 2002. This supercell also produced hail of a similar size (up to 4.5 cm) to the present case. The maxima in Z_{DR} and ρ_{hv} were also slightly removed from the maximum reflectivity values, as discussed above. It is important to only compare polarimetric data collected at similar heights in different storms because microphysical processes, such as the melting of hydrometeors, can strongly influence some of the polarimetric fields (e.g., Z_{DR}), making polarimetric variables vary considerably with height.

In summary, the Lipscomb County supercell of 23 May 2002 had prominent reflectivity wings of unknown origin. Like the storm itself, the reflectivity wings were long lasting and steadily increased in size during the observation period. Both the wings and the storm began a gradual weakening trend after 2342 UTC, but the wings maintained their size through 2359 UTC. The Z_{DR} and ρ_{hv} fields also showed agreement with those collected in other supercell storms in other studies. There was also good agreement between the Z_{DR} fields collected by the SPOL and XPOL radars, except for in the areas in which the XPOL beam was attenuated.

5. Dual-Doppler observations

The Lipscomb County storm maintains its supercell structure through the onset of dual-Doppler observations at 2345 UTC (Fig. 10a). The storm begins a slow weakening trend by 0000 UTC (Fig. 10b), such that by 0015 UTC (Fig. 10c), most of the classic supercell structure (e.g., the echo appendage and the large reflectivity gradient along its right flank) has disappeared. By 0030 UTC, only a small echo core greater than 40

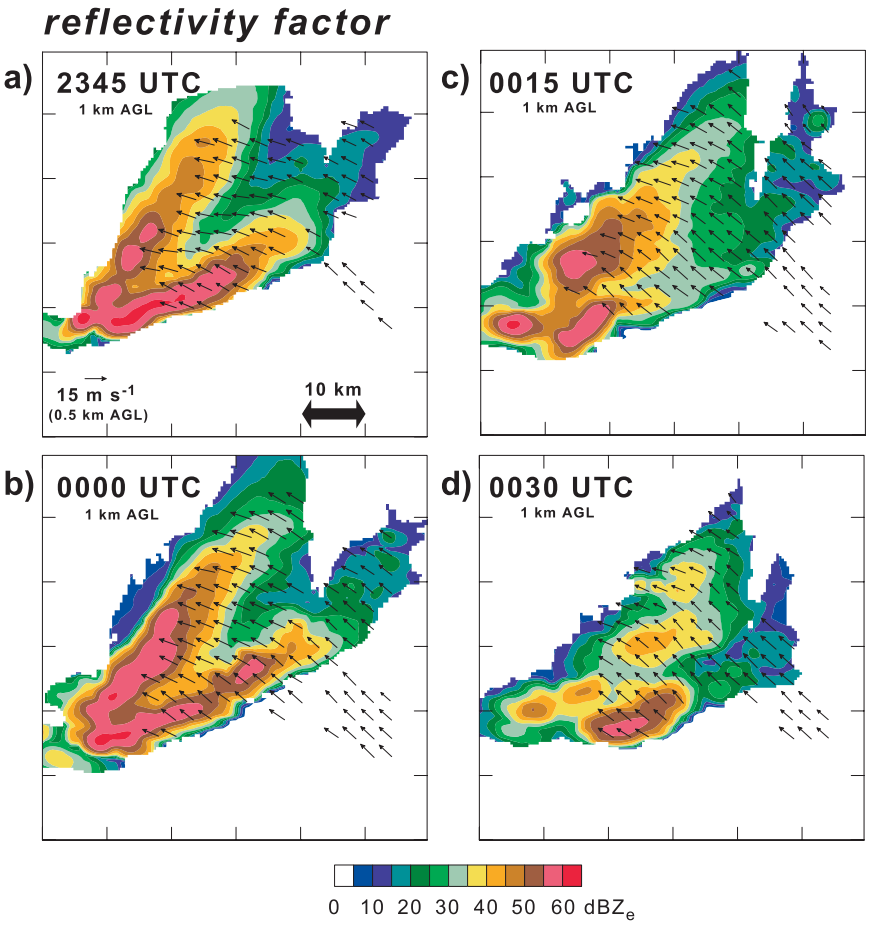

FIG. 10. Equivalent radar reflectivity factor (dBZ_e) at 1 km AGL observed by DOW2 at (a) 2345, (b) 0000, (c), 0015, and (d) 0030 UTC 23–24 May 2002. DOW2 raw reflectivities are uncalibrated; a correction of 8 dB was added to the fields shown above, based on comparisons with the SPOL and XPOL reflectivity observations. Dual-Doppler-derived storm-relative wind vectors at 0.5 km AGL also are shown.

dBZ_e remains (Fig. 10d), and the storm almost completely dissipates by 0100 UTC (not shown).

Throughout the analysis period, southeasterly storm-relative (s-r) winds are observed at low levels (0.4–1.0 km AGL) within the forward flank (e.g., Fig. 10). This s-r flow direction is a bit surprising given that previous observational (e.g., Wakimoto et al. 1996; Dowell and Bluestein 2002; Shabbott and Markowski 2006) and modeling studies (e.g., Fig. 1b) have found that air on the immediate cool side of the forward-flank gust front moves approximately parallel to the orientation of the forward-flank gust front. It is possible, however, that these differences arise from looking at the winds at 500 m AGL, as opposed to those closer to the ground.

Two sets of s-r trajectories, originating at different heights, were computed beginning at 2345 UTC, originating near and within the forward flank of the storm (Fig. 11). The zonal separation between the trajectories is 7–8 km, whereas the meridional separation is allowed to vary depending on the shape of the echo, but is generally on the order of 2–3 km. A trajectory was terminated when it reached a location with no dual-Doppler data. Trajectories beginning at 600 m AGL depict air parcels within the right reflectivity wing moving northwestward, farther into the main echo body. Trajectories originating at 850 m AGL, outside of the precipitation region, also move northwestward and eventually enter the higher reflectivity region associated with the right echo wing. These trajectories are consistent with both the s-r wind analysis (Fig. 10) and the raw single-Doppler data (not shown). The widespread southeasterly low-level flow throughout the forward flank suggests a lack of strong outflow in this region of the storm at this level.

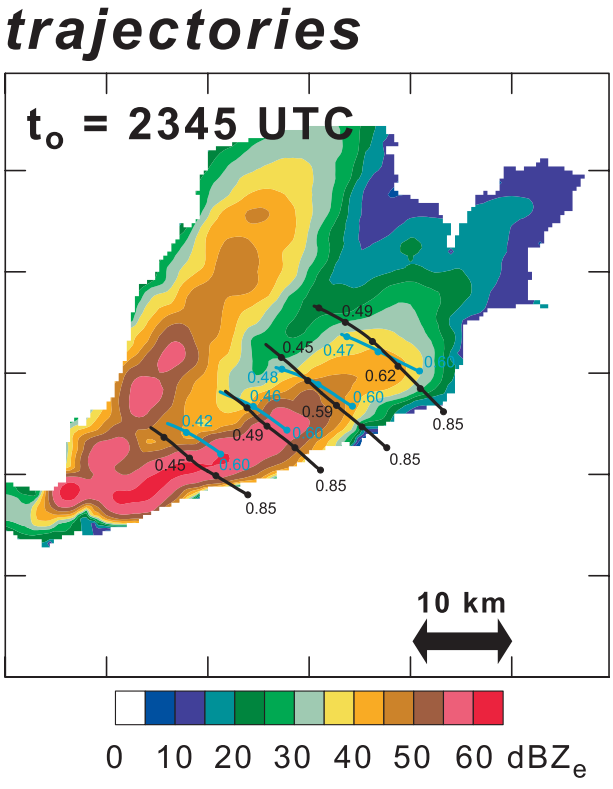

FIG. 11. Trajectories initiated at 2345 UTC 23 May 2002 at 0.85 km AGL immediately southeast of the precipitation region of the Lipscomb County supercell (black), and at 0.6 km AGL within the southern portion of the precipitation region (light blue). Markings appear along the trajectories at 5-min intervals, and altitudes of the trajectories in km AGL are indicated at select times. The trajectories are overlaid on the 2345 UTC reflectivity field (1 km AGL) observed by DOW2 (cf. Fig. 10a) and are plotted in the storm-relative reference frame. The trajectories are terminated where they exit the dual-Doppler data region.

All trajectories descend once they enter the main precipitation region, and eventually they descend so low that they pass beneath the radar horizon. An examination of the vertical velocity field (Fig. 12) reveals that a band of negative vertical velocities is approximately collocated with the southern reflectivity wing throughout the analysis period. Farther northwest, there is a band of upward vertical velocities approximately collocated with the weak-echo notch at 2345 UTC (Fig. 12a), which weakens and becomes less organized with time.

The vertical vorticity field at 2345 UTC (Fig. 13a) reveals a band of enhanced positive vorticity near the northern edge of the southern echo wing, which persists through 0000 UTC (Fig. 13b). Within this band, there are stronger vortices that are generally 2–3 km across. This band moves northwestward in an s-r sense, so that by 0015 UTC (Fig. 13c), it is located near the southern edge of the northern reflectivity wing. This band continues to move to the northwest through 0030 UTC (Fig. 13d), at which time it is located near the remnants of the northern wing of enhanced reflectivity.

The divergence field was analyzed to reveal the position of the gust front to the southeast of the main echo (e.g., Fig. 14). Its placement is based on the presence of a weak convergence maximum rather than a major wind shift because a major wind shift is not present. This feature is only present below about 1 km AGL, is rather diffuse, and it weakens with time such that it is indiscernible by 0015 UTC. Convergence is also visible in this region of the storm in the single-Doppler radial velocity data (not shown). A closer examination of the divergence field within the forward-flank echo region reveals several linear maxima and minima. It is possible that these features could be remnant horizontal convective rolls (given their linear orientation and spacing) that originated in the convective boundary layer ahead of the storm and have been advected into the precipitation region by the low-level flow. It is not possible from the current data and analysis to determine their origin for sure, however. It is unlikely that such features are artifacts of the analysis since they have appeared in different analyses that were obtained by using different synthesis methods in earlier versions of this work (not shown).

Like the low-level wind field, the low-level horizontal vorticity field in this storm also differs from some of the conceptual models of supercell thunderstorms. In many schematic models, the low-level vortex lines are oriented normal to the forward-flank gust front in the inflow south of the storm, then become oriented parallel to the gust front as they encounter it, such that they become directed toward the primary updraft of the storm (Fig. 1b). In this case, the low-level horizontal vorticity vector is nowhere oriented toward the storm's main updraft region (Fig. 15) near the forward-flank gust front. These vectors are consistent with the diffuse gust front noted above, and both of these observations suggest that only weak baroclinity is present in the forward flank of this storm. Throughout most of the northern and western portions of the storm, the horizontal vorticity vector points northwestward (Fig. 15a), although a northeastward orientation develops along the extreme southern flank of the storm by 0000 UTC (Fig. 15b). The horizontal vorticity field retains the same general pattern over the southern flank of the storm throughout the remainder of the observation period (Figs. 15c,d). Also, the line that marks the shift between a northeastward and northwestward orientation of the horizontal vorticity vector within the echo gradually moves northwestward with time, similar to the line of enhanced vertical vorticity discussed above. This

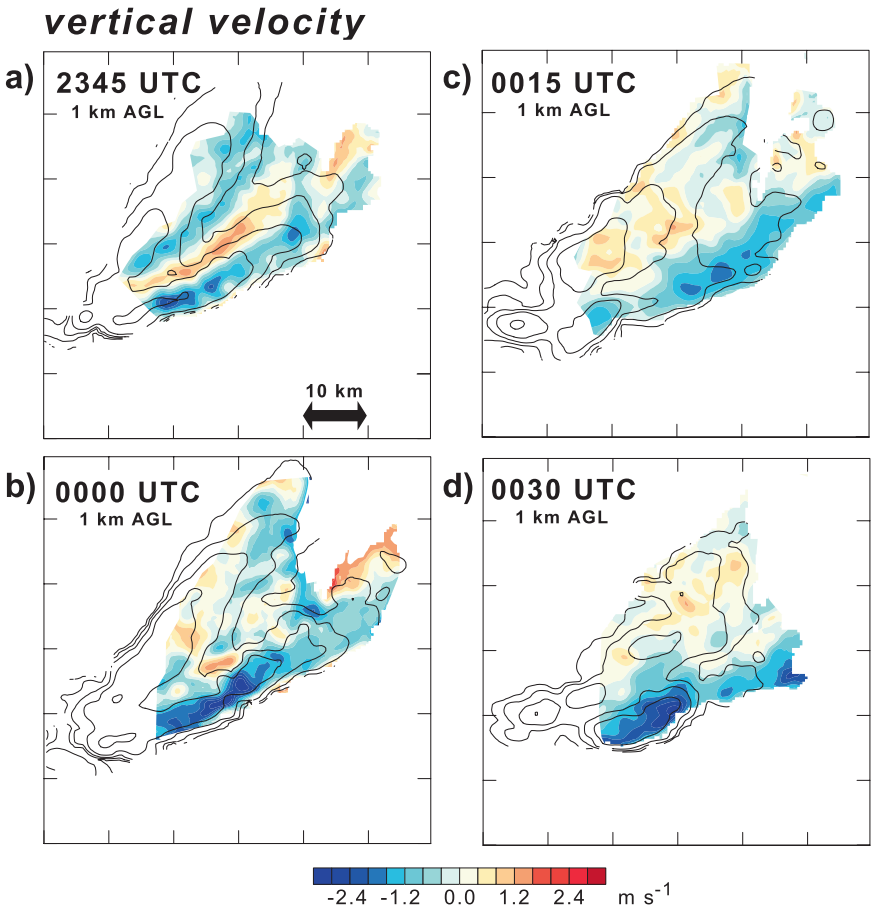

FIG. 12. Dual-Doppler-derived vertical velocity at 1 km AGL (color shading) at (a) 2345, (b) 0000, (c), 0015, and (d) 0030 UTC 23–24 May 2002. Contours of the DOW2 reflectivity field (cf. Fig. 10) are overlaid at 10-dBZ_e intervals.

same area is also roughly coincident with the weak-echo notch, a slight wind shift (Fig. 10), and the shift from weak downward to weak upward vertical velocities (Fig. 12). The horizontal vorticity vector outside of the precipitation region points approximately eastward (Fig. 15).[4]

Neither the low-level wind field (e.g., Fig. 10) nor the horizontal vorticity field (Fig. 15) suggests a large low-level buoyancy deficit within this storm. If that was the case, the horizontal vorticity vectors would likely point westward, not eastward, along the right flank of the storm. Buoyancy retrievals were also attempted and they did not reveal a substantial buoyancy deficit with this storm at any time (not shown). The trustworthiness of the retrievals was questionable, owing to a lack of strong temporal consistency; the retrievals were therefore omitted. Taken together, the above analyses also suggest the potential relative unimportance of baroclinic horizontal vorticity generation as a source of vertical vorticity for the low-level mesocyclone in this case. A comparison between the s-r wind field (Fig. 10) and the horizontal vorticity vector in the forward flank reveal no path to the updraft for any baroclinically generated horizontal vorticity, at least at levels above the radar horizon. Thus, if any baroclinically generated horizontal vorticity exists in this part of the storm, it cannot be tilted by the updraft and augment the vertical vorticity of the low-level mesocyclone. Similar differences between conceptual models and observations were found in the dual-Doppler study of Beck et al. (2006, see their Fig. 9). Trajectories computed by Ziegler et al. (2001),

[4] It is uncertain as to why the dual-Doppler-derived horizontal vorticity field does not match that obtained from the model sounding. Given that there were no upper-air observations in this region that would have been assimilated by LAPS, the finescale details in the LAPS hodograph are not always trustworthy. The hodograph is included to give a perspective of the "big picture" (e.g., the overall length and orientation of the hodograph from low to upper levels).

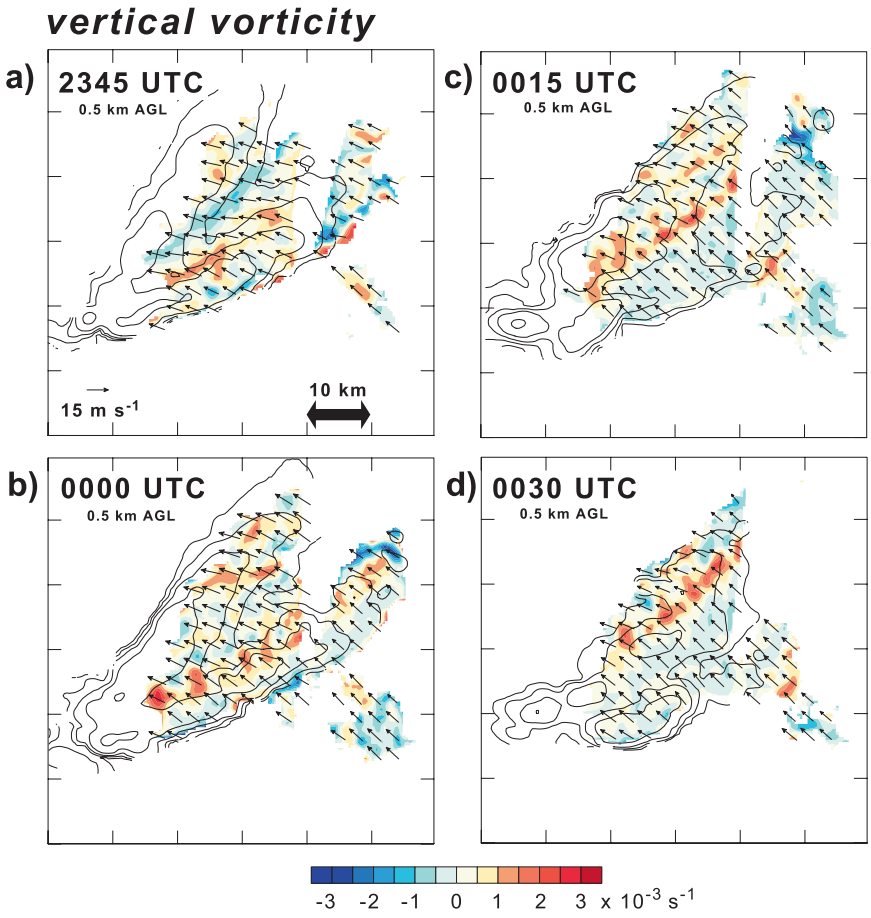

FIG. 13. Dual-Doppler-derived vertical vorticity at 0.5 km AGL (color shading) at (a) 2345, (b) 0000, (c), 0015, and (d) 0030 UTC 23–24 May 2002. Contours of the DOW2 reflectivity field (cf. Fig. 10) are overlaid at 10-dBZ_e intervals. Storm-relative wind vectors at 0.5 km AGL also are shown.

however, revealed that air parcels within the forward flank of a different storm flowed toward the updraft and mesocyclone regions of that storm, in close agreement with the conceptual models (see their Fig. 16). There is likely baroclinic vorticity generation occurring over the northern portions of the storm because the horizontal vorticity field in this part of the storm is so different from that observed in the ambient environment, but this vorticity is being advected northwestward, away from the updraft and mesocyclone. In fact, the low-level mesocyclone remained quite weak throughout the dual-Doppler analysis period, with the single-Doppler velocity couplet remaining less than 10 m s^{-1}.

Other studies have also suggested a somewhat reduced role of forward-flank baroclinity. For example, Shabbott and Markowski (2006) examined in situ thermodynamic observations from the forward flanks of both tornadic and nontornadic supercells and found that nontornadic supercells generally possess stronger baroclinity within their forward flanks than do tornadic ones. Although this result appears to be slightly counterintuitive, the authors note that a strong baroclinic zone implies a large density excess within the outflow, and a growing body of observations suggests that cold outflow is generally unfavorable for tornadogenesis (e.g., Markowski et al. 2002; Grzych et al. 2007). It is also possible that the outflow produced in some of the early supercell simulations may have been too cold because of the formulation of the vertical diffusion scheme at the lower boundary in some of the cloud models (Bryan et al. 2006), and the omission of both ice microphysics (e.g., Johnson et al. 1993) and radiation (Frame and Markowski 2006) in the models. There is probably a range of forward-flank cold pool strengths, with baroclinic generation of horizontal vorticity playing an important role in storms having strong cold pools, and with baroclinic processes being less important in storms having weak cold pools. Some past model studies may have exaggerated the importance of forward-flank cold pools and their attendant baroclinic generation because these models tended to produce too

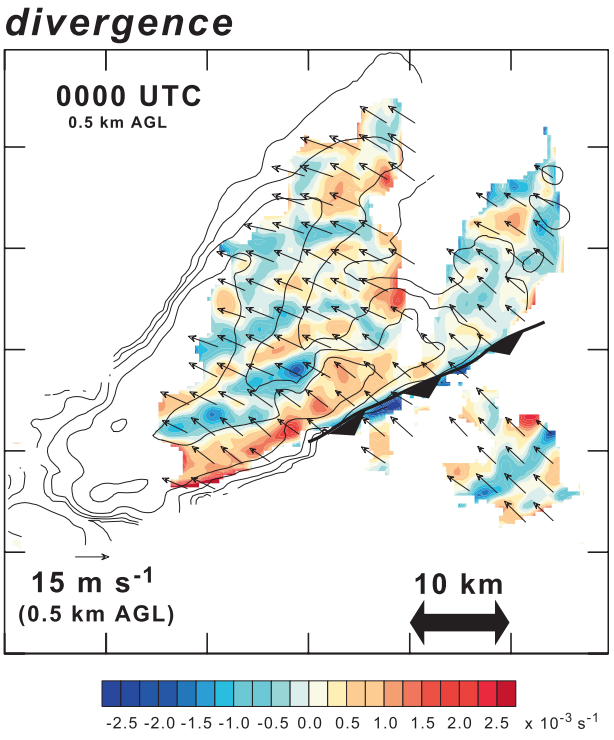

FIG. 14. Dual-Doppler-derived divergence at 0.5 km AGL at 0000 UTC. Storm-relative wind vectors at 0.5 km AGL also are shown. Contours of the DOW2 reflectivity field (cf. Fig. 10) are overlaid at 10-dBZ_e intervals. The thick line with filled barbs indicates the forward-flank gust front.

much cold air as noted above. The case discussed herein seems like a case with a weak cold pool. Photographs of supercells also suggest a wide range of opacity in forward-flank precipitation cores; some storms have highly opaque, dark cores while others have cores that are highly translucent. Unfortunately, there are no photographs of this storm at maturity.

6. Conclusions

The polarimetric and dual-Doppler observations of the 23 May 2002 Lipscomb County supercell presented herein allow the investigation of the hydrometeor distribution and the kinematic fields within the forward flank of a supercell thunderstorm. The radar observations suggest that neither hydrometeor size sorting nor storm splitting is responsible for the maintenance of the prominent winged reflectivity structure prevalent throughout the analysis period.

The three-dimensional wind syntheses indicate that air parcels within the forward-flank precipitation region generally do not flow into the updraft in the Lipscomb County storm, which differs from that portrayed in most conceptual models of supercell thunderstorms, wherein low-level streamlines originating in the forward-flank precipitation converge toward the updraft. The horizontal vorticity within this region is also not oriented toward the updraft. This suggests that baroclinic vorticity generation near the forward-flank gust front was probably not significant in this case. It is possible, however, that both the low-level wind and vorticity fields more closely matched the conceptual models outside the dual-Doppler domain, below the data horizon, or at an earlier stage in the storm's evolution, before the onset of dual-Doppler observations. It is also possible that the deviations from the conceptual models of a mature supercell noted above may have contributed to the weakness of the low-level mesocyclone in this case.

Nonetheless, this case study highlights the need for more finescale observations within all regions of supercell thunderstorms, not only the areas around the rear-flank downdraft and mesocyclone. Ideally, such a project would entail not only multiple Doppler radars, but also mobile probes (both airborne and ground based) capable of measuring the thermodynamic variables around and within the storm. From these observations, the range of characteristics of forward-flank downdrafts could be determined and their potential dynamical importance could be further evaluated.

Acknowledgments. We are grateful to all of the IHOP volunteers (too numerous to mention) who helped with the data collection, and to Marios Anagnostou and Manos Anagnostou for providing both the XPOL data and helpful comments regarding this work. We also thank John Gamache for sharing his variational wind synthesis technique and code; David Dowell for sharing some of his analysis code; and Steve Albers (ESRL), Chris Anderson (ESRL), Dan Birkenheuer (ESRL), Jim Marquis (PSU), John McGinley (ESRL), Brian Monahan (PSU), and Steve Williams (NCAR) for their assistance. Support from NSF Grants ATM-0437512 and ATM-0446509 is also acknowledged.

APPENDIX

Hydrometeor Classification Algorithm

For the purposes of this study, hydrometeor species are classified into bulk categories including hail, rain, dry graupel, dry snow aggregates, and a rain–wet hail mixture (which is the only mixture considered by this classification scheme). Furthermore, each category has subclassifications based on precipitation rate (e.g., heavy, moderate, or light), median hydrometeor size (e.g., giant,

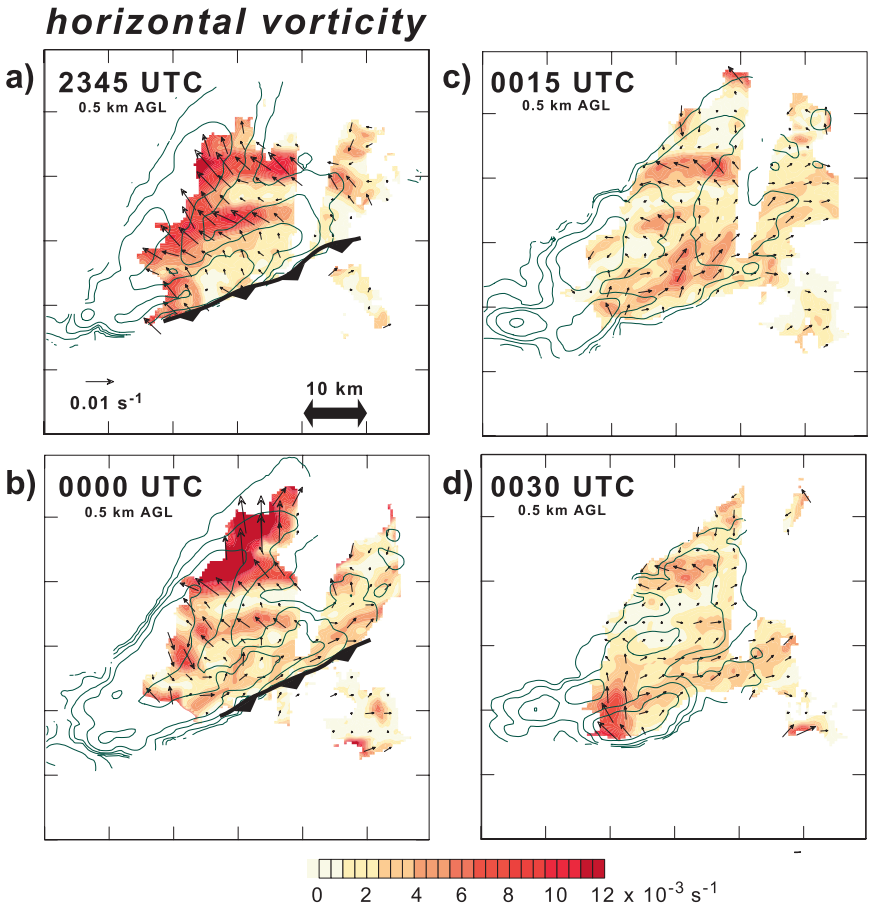

FIG. 15. Dual-Doppler-derived vertical horizontal vorticity vectors at 0.5 km AGL and magnitude (color shading) at (a) 2345, (b) 0000, (c), 0015, and (d) 0030 UTC 23–24 May 2002. Contours of the DOW2 reflectivity field (cf. Fig. 10) are overlaid at 10-dBZ_e intervals. The bold line with filled barbs indicates the forward-flank gust front.

large, or small), and wetness (e.g., wet or dry). In the case of snow crystals, an attempt is also made to discriminate between simple habits such as plates, columns, and needles. The polarimetric variables used to determine the dominant bulk hydrometeor types are described in Straka et al. (2000) and include reflectivity (Z_{HH}), differential reflectivity (Z_{DR}), specific differential phase (K_{DP}), linear depolarization ratio (LDR), the correlation coefficient between horizontally and vertically polarized waves (ρ_{hv}), air temperature (T), as well as numerous other calculated variables.

The decision process in the hydrometeor classification algorithm (HCA) is based on the principles of fuzzy logic (Straka 1996; Vivekanandan et al. 1999; Straka et al. 2000; Liu and Chandrasekar 2000; Zrnic et al. 2001). Various basis functions such as sigmoids, Gaussians, bell shapes, rectangles, and other shapes are used to define ''confidence factors,'' which have magnitudes ranging between zero and one. These confidence factors approximate the degree to which the observed values of the polarimetric variables represent each hydrometeor type. All of the basis functions are trapezoids in the analyses presented herein. Thresholds, given by Straka et al. (2000), define regions in the radar variable parameter space where the confidence factors for the fuzzy logic basis functions are equal to 0.5, thereby enabling the determination of each hydrometeor type. The centroids of all of the confidence factors are then used to determine the dominant bulk hydrometeor types suggested by the data. Table A1 lists a sample of some of the values used to discriminate between hydrometeor classifications in the analyses herein. It is important to note that there are also other calculated variables used and that multidimensional parameter spaces are used throughout this algorithm (Z_{HH} and Z_{DR}, Z_{DR} and LDR, Z_{HH} and K_{DP}, etc.).

One potential difficulty of using bulk hydrometeor classification algorithms with polarimetric radar data is

TABLE A1. Polarimetric values for classification of hydrometeors. Numbers represent a confidence factor of 0.5.

Hydrometeor type	Z_{HH} (dBZ)	Z_{DR} (dB)	K_{DP} (° km^{-1})	ρ_{hv}	LDR (dB)
Hail	45–80	−2–0.5	−0.5–1	<0.97	>−26
Rain–wet hail	45–80	−1–6	>0	<0.95	>−25
Dry graupel	20–50	−0.5–2	0–1.5	>0.95	<−20
Dry snow	<35	0–1	0–0.2	>0.95	<−25
Rain	<60	>0	>0	>0.95	<−25
Small raindrops	<28	0–0.7	0–0.03	>0.97	<−32
Medium raindrops	28–44	0.7–2.0	0.03–0.60	>0.95	−34 to −28
Large raindrops	44–60	>2	>0.6	>0.95	−30 to −25

that the signatures of the various hydrometeor types are not always unique. Rather, in most cases, there is at least some overlap between the parameter spaces of the various hydrometeor types. In these instances, fuzzy logic plays a powerful role in deciding which hydrometeor species is likely the dominant one. Occasionally, the confidence factors for the primary hydrometeor choice may not identify the dominant hydrometeor species correctly, and the secondary hydrometeor choice may be correct, leading to misclassifications. These can be minimized through neighbor comparisons. For example, if the majority of a group's neighbors are more like the secondary bulk hydrometeor category than the primary one, the secondary hydrometeor choice is used. If a hydrometeor classification cannot be made from the polarimetric data (e.g., due to missing data or ambiguous results), then a combination of the reflectivity and temperature fields are used to made admittedly crude approximations.

Some of the difficulties in developing procedures to use polarimetric radar data to deduce dominant bulk hydrometeor types and amounts result from (i) a lack of a thorough understanding of radar signatures of specific bulk hydrometeor types and mixtures; (ii) a need for information about hydrometeor size distributions (and other characteristics) during free fall; (iii) a means to circumvent problems with ambiguous bulk hydrometeor classifications (e.g., when either more than one or no bulk hydrometeor type is suggested); (iv) a need for complete sets of both qualitative and quantitative hydrometeor observations for rigorous comparisons to the results of this classification algorithm; (v) a lack of adequate identification of artifacts in the radar data; and (vi) a lack of understanding uncertainties in radar calibration. Thus, continuing efforts to change and adapt existing algorithms must be done using in situ aircraft data to make further improvements in hydrometeor classification using polarimetric radar data.

REFERENCES

Alexander, C. R., and J. M. Wurman, 2005: The 30 May 1998 Spencer, South Dakota storm. Part I: The structural evolution and environment of the tornadoes. *Mon. Wea. Rev.,* **133,** 72–97.

Barnes, S. L., 1964: A technique for maximizing details in numerical weather map analysis. *J. Appl. Meteor.,* **3,** 396–409.

Beck, J. R., J. L. Schroeder, and J. M. Wurman, 2006: High-resolution dual-Doppler analyses of the 29 May 2001 Kress, Texas, supercell. *Mon. Wea. Rev.,* **134,** 3125–3148.

Bluestein, H. B., W. P. Unruh, D. C. Dowell, T. A. Hutchinson, T. M. Crawford, A. C. Wood, and H. Stein, 1997: Doppler radar observations of the Northfield, Texas, tornado of 25 May 1994. *Mon. Wea. Rev.,* **125,** 212–230.

——, C. C. Weiss, and A. L. Pazmany, 2003: Mobile Doppler radar observations of a tornado in a supercell near Bassett, Nebraska, on 5 June 1999. Part I: Tornadogenesis. *Mon. Wea. Rev.,* **131,** 2954–2967.

Bryan, G. H., J. C. Knievel, and M. D. Parker, 2006: A multimodel assessment of RKW theory's relevance to squall-line characteristics. *Mon. Wea. Rev.,* **134,** 2772–2792.

Craven, J. P., R. E. Jewell, and H. E. Brooks, 2002: Comparison between observed convective cloud-base heights and lifting condensation level for two different lifted parcels. *Wea. Forecasting,* **17,** 885–890.

Davies-Jones, R. P., 1979: Dual-Doppler radar coverage area as a function of measurement accuracy and spatial resolution. *J. Appl. Meteor.,* **18,** 1229–1233.

Doswell, C. A., III, and E. N. Rasmussen, 1994: The effect of neglecting the virtual temperature correction on CAPE calculations. *Wea. Forecasting,* **9,** 625–629.

Doviak, R. J., and D. S. Zrnic, 1993: *Doppler Radar and Weather Observations*. Academic Press, 562 pp.

Dowell, D. C., and H. B. Bluestein, 2002: The 8 June 1995 McLean, Texas, storm. Part I: Observations of cyclic tornadogenesis. *Mon. Wea. Rev.,* **130,** 2626–2648.

Frame, J., and P. Markowski, 2006: Simulations of a supercell thunderstorm with radiative transfer, surface physics, and a soil model. Preprints, *23rd Conf. on Severe Local Storms,* St. Louis, MO, Amer. Meteor. Soc., 16.6. [Available online at http://ams.confex.com/ams/pdfpapers/115442.pdf.]

Gamache, J. F., 1997: Evaluation of a fully three-dimensional variational Doppler analysis technique. Preprints, *28th Conf. on Radar Meteorology,* Austin, TX, Amer. Meteor. Soc., 422–423.

Grzych, M. L., B. D. Lee, and C. A. Finley, 2007: Thermodynamic analysis of supercell rear-flank downdrafts from project ANSWERS. *Mon. Wea. Rev.,* **135,** 240–246.

Heinselman, P. L., and A. V. Ryzhkov, 2006: Validation of polarimetric hail detection. *Wea. Forecasting,* **21,** 839–850.

Johnson, K. D., P. K. Wang, and J. M. Straka, 1993: Numerical simulations of the 2 August 1981 CCOPE supercell storm with and without ice microphysics. *J. Appl. Meteor.,* **32,** 745–759.

Klemp, J. B., 1987: Dynamics of tornadic thunderstorms. *Annu. Rev. Fluid Mech.,* **19,** 369–402.

——, and R. Rotunno, 1983: A study of the tornadic region within a supercell thunderstorm. *J. Atmos. Sci.,* **40,** 359–377.

Lee, W.-C., and J. M. Wurman, 2005: Diagnosed three-dimensional axisymmetric structure of the Mulhall tornado on 3 May 1999. *J. Atmos. Sci.,* **62,** 2373–2393.

Lemon, L. R., and C. A. Doswell III, 1979: Severe thunderstorm evolution and mesocyclone structure as related to tornadogenesis. *Mon. Wea. Rev.,* **107,** 1184–1197.

Liu, H., and V. Chandrasekar, 2000: Classification of hydrometeors based on polarimetric radar measurements: Development of fuzzy logic and neuro-fuzzy systems, and in situ verification. *J. Atmos. Oceanic Technol.,* **17,** 140–164.

Lutz, J., P. Johnson, B. Lewis, E. Loew, M. Randall, and J. VanAndel, 1995: NCAR's S-Pol: Portable polarimetric S-band radar. Preprints, *Ninth Symp. on Meteorological Observations and Instrumentation,* Charlotte, NC, Amer. Meteor. Soc., 408–410.

Markowski, P. M., J. M. Straka, and E. N. Rasmussen, 2002: Direct surface thermodynamic observations within the rear-flank downdrafts of nontornadic and tornadic supercells. *Mon. Wea. Rev.,* **130,** 1692–1721.

NCDC, 2002: *Storm Data*. Vol. 44, No. 5, 414 pp.

Pauley, P. M., and X. Wu, The theoretical, discrete, and actual response of the Barnes objective analysis scheme for one- and two-dimensional fields. *Mon. Wea. Rev.,* **118,** 1145–1164.

Rotunno, R., and J. B. Klemp, 1985: On the rotation and propagation of simulated supercell thunderstorms. *J. Atmos. Sci.,* **42,** 271–292.

Ryzhkov, A. V., T. J. Schuur, D. W. Burgess, and D. S. Zrnic, 2005: Polarimetric tornado detection. *J. Appl. Meteor.,* **44,** 557–570.

Shabbott, C. J., and P. M. Markowski, 2006: Surface in situ observations within the outflow of forward-flank downdrafts of supercell thunderstorms. *Mon. Wea. Rev.,* **134,** 1422–1441.

Straka, J. M., 1996: Hydrometeor fields in supercell storms as deduced from dual-polarization radar. Preprints, *18th Conf. on Severe Local Storms,* San Francisco, CA, Amer. Meteor. Soc., 551–554.

——, D. S. Zrnic, and A. V. Ryzhkov, 2000: Bulk hydrometeor classification and quantification using polarimetric radar data: Synthesis of relations. *J. Appl. Meteor.,* **39,** 1341–1372.

Trapp, R. J., 1999: Observations of nontornadic low-level mesocyclones and attendant tornadogenesis failure during VORTEX. *Mon. Wea. Rev.,* **127,** 1693–1705.

——, and C. A. Doswell III, 2000: Radar data objective analysis. *J. Atmos. Oceanic Technol.,* **17,** 105–120.

Vivekanandan, J., S. M. Ellis, R. Oye, D. S. Zrnic, A. V. Ryzhkov, and J. M. Straka, 1999: Cloud microphysics retrieval using S-band dual-polarization radar measurements. *Bull. Amer. Meteor. Soc.,* **80,** 381–387.

Wakimoto, R. M., 2001: Convectively driven high wind events. *Severe Convective Storms, Meteor. Monogr.,* No. 50, Amer. Meteor. Soc., 255–298.

——, and H. Cai, 2000: Analysis of a nontornadic storm during VORTEX 95. *Mon. Wea. Rev.,* **128,** 565–592.

——, W.-C. Lee, H. B. Bluestein, C.-H. Liu, and P. H. Hildbrand, 1996: ELDORA observations during VORTEX 95. *Bull. Amer. Meteor. Soc.,* **77,** 1465–1481.

——, C. Liu, and H. Cai, 1998: The Garden City, Kansas, storm during VORTEX 95. Part I: Overview of the storm's life cycle and mesocyclogenesis. *Mon. Wea. Rev.,* **126,** 372–392.

——, H. V. Murphey, D. C. Dowell, and H. B. Bluestein, 2003: The Kellerville tornado during VORTEX: Damage survey and Doppler radar analysis. *Mon. Wea. Rev.,* **131,** 2197–2221.

Weckwerth, T. M., and Coauthors, 2004: An overview of the International H2O Project (IHOP_2002) and some preliminary highlights. *Bull. Amer. Meteor. Soc.,* **85,** 253–277.

Wicker, L. J., and R. B. Wilhelmson, 1995: Simulation and analysis of tornado development and decay within a three-dimensional supercell thunderstorm. *J. Atmos. Sci.,* **52,** 2675–2703.

Wurman, J. M., 2001: The DOW Multiple-Doppler Network. Preprints, *30th Int. Conf. on Radar Meteorology,* Munich, Germany, Amer. Meteor. Soc., 95–97.

——, and S. Gill, 2000: Finescale radar observations of the Dimmitt, Texas (2 June 1995), tornado. *Mon. Wea. Rev.,* **128,** 2135–2164.

——, J. M. Straka, E. N. Rasmussen, M. Randall, and A. Zahrai, 1997: Design and deployment of a portable, pencil-beam, pulsed, 3-cm Doppler radar. *J. Atmos. Oceanic Technol.,* **14,** 1502–1512.

——, Y. P. Richardson, C. R. Alexander, S. Weygandt, and P. F. Zhang, 2007a: Dual-Doppler and single-Doppler analysis analysis of a tornadic storm undergoing mergers and repeated tornadogenesis. *Mon. Wea. Rev.,* **135,** 736–758.

——, ——, ——, ——, and ——, 2007b: Dual-Doppler analysis of winds and vorticity budget terms near a tornado. *Mon. Wea. Rev.,* **135,** 2392–2405.

Ziegler, C. L., E. N. Rasmussen, T. R. Shepherd, A. I. Watson, and J. M. Straka, 2001: The evolution of low-level rotation in the 29 May 1994 Newcastle-Graham, Texas, storm complex during VORTEX. *Mon. Wea. Rev.,* **129,** 1339–1368.

Zrnic, D. S., A. V. Ryzhkov, J. M. Straka, Y. Liu, and J. Vivekanandan, 2001: Testing a procedure for automatic classification of hydrometeor types. *J. Atmos. Oceanic Technol.,* **18,** 892–913.